Journal of Power Sources 628 (2025) 235808

Contents lists available at ScienceDirect

Journal of Power Sources

journal homepage: www.elsevier.com/locate/jpowsour

The exploitation of eigenspectra in electrochemical impedance spectroscopy: Reconstruction of spectra from sparse measurements

Christian Mänken [a,b,*], Dominik Schäfer [a], Rüdiger-A. Eichel [a,b]

[a] Institute of Energy Technologies - Fundamental Electrochemistry (IET-1), Forschungszentrum Jülich GmbH, 52428 Jülich, Germany
[b] Institute of Physical Chemistry, RWTH Aachen University, 52074 Aachen, Germany

GRAPHICAL ABSTRACT

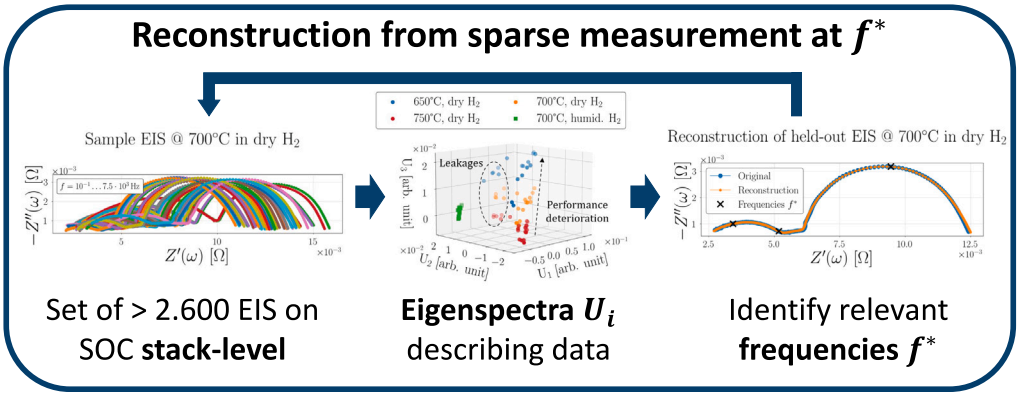

HIGHLIGHTS

- Dominant patterns found in set of over 2,600 EIS conducted on SOC stacks.
- Patterns sufficient for low-dimensional description and accurate reconstruction of EIS.
- Reconstruction of EIS from sparse measurements exploiting the determined patterns.
- Identification of 2-6 optimal frequencies for reconstruction at varying meas. conditions.
- Corrupted/distorted EIS can be reconstructed sampling only at optimal frequencies.

ARTICLE INFO

Keywords:
Electrochemical impedance spectroscopy
Solid oxide cell stacks
Reconstruction from sparse measurements
Optimal sensor placement
On-board diagnostics

ABSTRACT

Electrochemical Impedance Spectroscopy (EIS) represents one of the most widely utilized techniques for the characterization of solid oxide cells (SOCs) and stacks in contemporary research. This work examines patterns in a set X of over 2,600 EIS measurements conducted on SOC stack level to identify a low-dimensional representation of the data. Besides the efficient training of data-driven models in such, this work primarily focuses on enabling the reconstruction of complete spectra from sampling the impedance at a limited number of relevant frequencies, thus significantly reducing the measurement time. By applying singular value decomposition, a reconstruction matrix can be developed containing a set of r patterns to sufficiently describe all the EIS in X. Based on these patterns, a set of $r/2$ tailored frequencies can be determined. For every permutation of measurement conditions in X and for r between four and twelve, the reconstruction results are

* Corresponding author at: Institute of Energy Technologies - Fundamental Electrochemistry (IET-1), Forschungszentrum Jülich GmbH, 52428 Jülich, Germany.
E-mail address: c.maenken@fz-juelich.de (C. Mänken).

https://doi.org/10.1016/j.jpowsour.2024.235808
Received 11 September 2024; Received in revised form 29 October 2024; Accepted 6 November 2024
Available online 2 December 2024

comprehensively discussed utilizing EIS measurements conducted on a holdout SOC stack and thus not being part of the data set X. Furthermore, EIS containing varying faults and artificially distorted EIS are used to also capture unforeseen behavior. Depending on the measurement conditions accurate reconstructions can be reported for $r = 6$, i.e. three tailored frequencies.

1. Introduction

EIS is ubiquitous for performance assessment and degradation analysis in electrochemical converters, such as SOC single cells and stacks [1]. However, the comparatively long measurement time and the relatively high costs preclude the application of standard EIS techniques such as sine sweep for diagnosis of SOC stacks in industrial applications. For the diagnosis and State-of-Charge estimation of batteries, there exist measurement techniques employing Pseudo-random Binary Sequence (PRBS) [2,3] input signals or Pulse Impedance Spectroscopy (PIS) [4] to significantly shorten the necessary measurement time. As an early stage monitoring method PRBS was applied in [5] to detect faulty operation modes, namely fuel starvation, leakage and carbon deposition. Further, in [6] a random binary sequence with discrete switching times was applied to monitor temporal fuel starvation during a 3,600 h SOC stack experiment. The main advantage of EIS based on PRBS excitation signals is a significant reduction in measurement time which in both cases was successfully demonstrated. However, these techniques still require an elaborated excitation signal together with the corresponding hardware capable of processing broadband signals. In the case of devices under test (DUTs) that do not undergo fundamental changes in their material and geometric properties, such as mass-produced SOC stacks, an alternative approach to facilitating EIS measurements may be to focus on the output signal rather than the input signal. If it can be demonstrated that a set of EIS measurements conducted on several identical or at least similar DUTs via sine sweep measurements exhibits dominant and recurrent patterns, it may be possible to reconstruct the data from sparse EIS measurements at specific frequencies only. This would result in a notable reduction in the time required for measurements and would also avoid the need for broadband-capable hardware. The approximation of data from few measurements exploiting data-inherent patterns is closely related to the field of optimal sensor location in general and reconstruction from sparse measurements [7] in particular. In a concise overview, [7] presents an analysis of applications and methods. One illustrative instance of this methodology in an entirely distinct engineering domain is its application to reconstructing flow fields based on a limited set of measurements as investigated in [8]. In their study, the authors observed a significantly enhanced estimation of vortex shedding past a cylinder at low Reynolds number, when comparing to traditional methods, e.g. least squares regression. The reconstruction quality was observed to outperform latter method even when noise or corrupted measurements were present. In terms of the present task, this would entail a reduction in the number of necessary sine sweep measurements, which are relatively straightforward to conduct. This could potentially result in a rapid and cost-effective alternative to conventional EIS measurements. However, such methods are contingent upon the existence of dominant data-inherent patterns in a set of measurements that are intended to be sampled sparsely. These patterns can be determined by means of Principal Component Analysis (PCA) [9], Proper Orthogonal Decomposition (POD) [10], or, as applied in this work, by means of the Singular Value Decomposition (SVD) [11, pp. 4]. An advantageous property of the SVD is the provision of an optimal rank-r approximation of a data matrix X by only considering the first r singular values and discarding the rest, thus yielding a low-dimensional representation of data [11, pp. 8]. The number of required point sensors for reconstruction from sparse measurements using the SVD is directly linked to the rank r as shown in [7], which is why the determination of an appropriate threshold for the rank is utterly important for this method. In general, there exist various methods to do so. One conventional approach is to truncate the singular values at a specific value for the cumulative energy content, for instance greater than 90% or 99% [11, pp. 34]. Another method is to select the threshold in a way ensuring that the condition number of the singular values containing matrix assumes a specific value, as exemplified by [12]. In contrast, [13] proposed a method to find the optimal threshold under the assumption that the low-rank structure of a data matrix contains Gaussian white noise. A comparison of these methods to find the optimal threshold will be given for low-rank approximations of a set of over 2.600 EIS measurements conducted on SOC stacks at Forschungszentrum Jülich. Thus, a set of holdout measurements conducted at various measurement conditions but on a separate DUT with similar material properties could accurately be reconstructed from sampling the impedance, depending on the measurement condition, at only three to six frequencies. The optimal frequencies for impedance sampling are estimated for each measurement condition individually and for all measurement conditions combined. Moreover, the information-rich features embedded in low-rank approximations derived from the SVD have been successfully deployed in diverse domains of fuel cell modeling. For instance, low-rank approximations have been employed for the diagnosis of faults in polymer electrolyte membrane (PEM) fuel cells, as demonstrated in [14]. Additionally, they have been utilized for the experimental parameterization of a PEM fuel cell stack, wherein the simultaneous estimation of multiple structured state space models was conducted [15]. The suitability of the determined low-rank features, in the present work referred to as eigenspectra, for identification of distinct degradation states and recurrent fault patterns is investigated, as well. In future work the focus will be on application of the found patterns in machine learning (ML) frameworks for performance prediction. The reconstruction quality is also verified for EIS containing unforeseen peculiarities, with sampling of the impedance at those frequencies determined to be optimal. This includes the introduction of artificially induced distortions via equivalent circuit modeling (ECM) and EIS in the presence of known faults, such as a loss of contact on one layer of the stack.

2. Data and methods

2.1. Consolidation of the EIS data set

In recent years several SOC stack experiments have been conducted at Forschungszentrum Jülich utilizing the standard Jülich F10 design [16,17] comprising fuel electrode supported half-cells by the manufacturer elcogen (Tallinn, Estonia), some with in-house screen printed air electrodes. The stacks have been subjected to a variety of operational modes over different durations of operation, but consistently for the purpose of degradation science. 16 of these experiments were identified as suitable for the scope of this work, with further information given on them in Section S1. The consolidated experiments comprise approximately 47,000 h of operation and over 2.600 individual EIS spectra, in total. In addition, the EIS measurements conducted on a further holdout stack experiment were used for validation. All EIS measurements were conducted on each individual stack layer and on stack level (sum of layer measurements) at specific stages of the experiments. Further, all measurements were conducted in galvanostatic mode, usually with 5 A DC and 2 A AC excitation and only in few cases deviating towards larger DC currents and smaller AC currents, respectively. Similarly, the gas flows were usually kept at standardized values ($\dot{V}_n = 1.1\,\mathrm{l\,min^{-1}}$ of H_2 or H_2O depending on operating mode plus

additional feed gas and $\dot{V}_n = 41\,\mathrm{min}^{-1}$ of air per stack layer).[1] The stack temperatures varied between 650°C and 800°C. Further, the majority of measurements was conducted in fuel cell mode, but several measurements were also conducted in electrolysis and few also in co-electrolysis mode. Thus, the consolidated set of EIS measurements provides a comprehensive overview of degradation stages and minor fault patterns on SOC stack level in a range of measurement conditions. To compensate for recurrent instabilities such as minor temperature drifts or parasitic, inductive impedance, the set of EIS measurements has been curated using the proposed procedure shown in [18]. As a result of the Linear Kramers–Kronig validity test, high-frequency impedance exhibiting large residual errors is omitted in some measurements, resulting in spectra with a reduced maximum frequency. Furthermore, the number of frequencies per measurement decade at which the impedance was determined varies across the entire data set. The first peculiarity can be remedied by reducing the maximum considered frequency of all measurements. The second point, however, requires a re-sampling of the measurements due to subsequent data handling in large matrices that use a consistent frequency range as an index. A cubic spline approximation has been applied to all measurements to interpolate to a consistent range of 50 frequencies per measurement decade in the range between 0.1 Hz and the respective highest frequency, but maximum 50 kHz. The number of frequencies per measurement decade was chosen upon the majority of measurements. The magnitude and phase of the impedance were separately interpolated, and the resulting values were used to form the complex impedance. With regard to degradation analysis, the time under load, respectively time under temperature at the date of the EIS measurement and the measurement conditions are important. Therefore, Fig. 1 illustrates the latter together with the distribution of frequencies that the measurements in the data set comprise. For this overview, the measurements were attributed to the closest temperatures, however, by far the most were conducted at 700°C. A significant number of measurements has been conducted in humidified H_2, typically with 20% steam content. Furthermore, most of the measurements were taken with a duration of less than 6,000 h, whereby *under current* or *under temperature* means the actual time in load operation or in the heated oven, as all experiments were conducted in furnaces. Some of the measurements were conducted at beyond 12,000 h under load and temperature, respectively. Conclusively, Fig. 1 also depicts the aforementioned fraction of spectra exhibiting a certain usable maximum frequency. As illustrated 49.9% of the impedance spectra exhibit a maximum frequency of 25 kHz, 86.8% reach 15 kHz and all spectra in the consolidation show a maximum frequency of 7.5 kHz. To utilize the majority of measurements and taking into account the comparably low information content at high frequencies, inter alia, due to lower signal to noise ratio (SNR) in spectra conducted on stack level, it is reasonable to neglect the frequencies above 7.5 kHz. The range of frequencies logarithmically distributed with 50 steps per decade between 0.1 Hz and 7.5 kHz is abbreviated with $\hat{f}$ within this work. The set of curated and pre-processed EIS measurements is vectorially concatenated into a large data matrix $X \in \mathbb{R}^{n\times m}$ for further data analysis. In addition, the real Z' and imaginary part Z'' of the impedance are vertically stacked to obtain a matrix with rational values only, as exemplified in Eq. (1). The horizontal arrangement of the individual spectra in the form of column vectors is purely chosen in the chronological order of the performed experimental characterizations and is therefore arbitrary. For the set of curated and pre-processed EIS measurements, the number of individual spectra assumes a value of $m = 2.610$, while $n = 2|\hat{f}| = 488$:

$$X = \begin{bmatrix} Z'_{0.1\,\mathrm{Hz},1} & Z'_{0.1\,\mathrm{Hz},2} & \cdots \\ \vdots & \ddots & \vdots \\ Z'_{7.5\,\mathrm{kHz},1} & \cdots & Z'_{7.5\,\mathrm{kHz},m} \\ Z''_{0.1\,\mathrm{Hz},1} & Z''_{0.1\,\mathrm{Hz},2} & \cdots \\ \vdots & \ddots & \vdots \\ Z''_{7.5\,\mathrm{kHz},1} & \cdots & Z''_{7.5\,\mathrm{kHz},m} \end{bmatrix} \in \mathbb{R}^{n\times m},\ f_i \in \hat{f} \tag{1}$$

[1] $T_n = 273,15\,\mathrm{K}$ and $p_n = 101325\,\mathrm{Pa}$.

for the chosen frequency range and number per measurement decade, respectively. All EIS conducted on a specific stack experiment, namely F1004-139 (cf. Section S1) were excluded from the main analysis and are referred to throughout this work for the purpose of validation. The data handling and evaluation is conducted with Python 3.9 and selected frameworks and libraries [19,20].

2.2. Determination of dominant patterns in the data set

In the literature, there exists a number of suitable methods for dimension reduction via identification of predominant patterns often referred to as latent spaces. In this work, the focus is on the application of the singular value decomposition (SVD), which is comprehensively described in [11, pp. 4]. The SVD is suitable to determine an optimal and unique rank-r approximation of high-dimensional data by exploiting dominant patterns. In addition to numerical stability, the SVD is guaranteed to exist, unlike eigen-decompositions [11, pp. 4]. The SVD is applied to the consolidated EIS data matrix $X \in \mathbb{R}^{n\times m}$, which was mean centered beforehand by subtracting the mean spectrum $\bar{x}$:

$$X = U\Sigma V^T \tag{2}$$

$U \in \mathbb{R}^{n\times n}$ and $V \in \mathbb{R}^{m\times m}$ are unitary matrices with orthonormal columns, and $\Sigma \in \mathbb{R}^{n\times m}$ is a matrix with real, non-negative entries on the diagonal and zeros off the diagonal [11, p. 5]. While the columns of U and V are referred to as the right, respectively left singular vectors, the diagonal elements of Σ, arranged in descending order, are called singular values. Given the centrality of impedance spectra to this work, it is reasonable to designate the column vectors in U as *eigenspectra*. A rank-r approximation of the EIS data matrix X denoted as $\widetilde{X}$ is feasible by only considering the first r singular values, thus the first r columns and rows in U and V^T, respectively. Thus, a significant dimensional reduction of the EIS data can be achieved by a low-rank approximation:

$$\widetilde{X} = U_\mathrm{r}\Sigma_\mathrm{r}V_\mathrm{r}^T \tag{3}$$

The proof of the optimal approximation is provided by the Eckart-Young theorem [21]. Therefore, the approximation by means of the dyadic summation of Eq. (3) provides, for a given rank r, the best approximation of X considering the l^2-norm [11, p. 8]:

$$\widetilde{X} = \sum_{k=1}^{r} \sigma_k u_k v_k^T \tag{4}$$

Based on this, the matrix U_r containing the eigenspectra represents a reconstruction basis by which all measurements contained in X can be transformed into a r-dimensional space. This does also apply to measurements acquired on additional DUTs not included in X, as will be shown for EIS conducted on a holdout validation stack under comparable measurement conditions. Therefore, a new measurement x^* is transformed by mean-centering of the measurement and multiplication with U_r^T (cf. Eq. (5)), whereby a unique *fingerprint* of this measurement is determined in the reconstruction basis U_r. A further multiplication by U_r and addition of the mean spectrum $\bar{x}$ results in the high-dimensional reconstruction $\widetilde{x^*}$ of the original measurement:

$$\widetilde{x^*} = \bar{x} + U_\mathrm{r}U_\mathrm{r}^T(x^* - \bar{x}) \tag{5}$$

Consequently, the quality of the approximation of a specific measurement $\widetilde{x}$, given a data set X, is only dependent upon the rank r of the reconstruction basis U_r. In turn, for the choice of the rank r the importance of individual eigenspectra U_i must be considered. As described above, the latter is given by the singular values σ_i arranged in descending order. One method for determining an optimal threshold for rank r is to truncate at that rank which encompasses 90% or 99% of the variance or energy content in the data, as indicated by the cumulative sum of the singular values [11, pp. 34]. An alternative approach is to

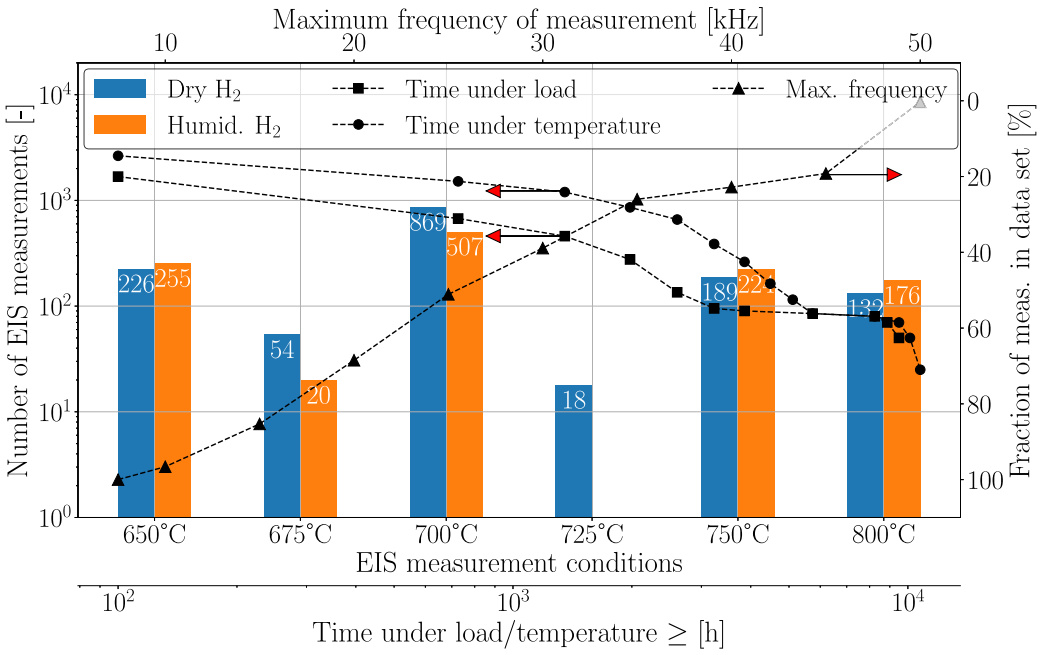

Fig. 1. Statistic description of EIS data set by means of measurement conditions, duration under load/temperature at measurement time and fraction of measurements comprising a certain maximum frequency after curation.

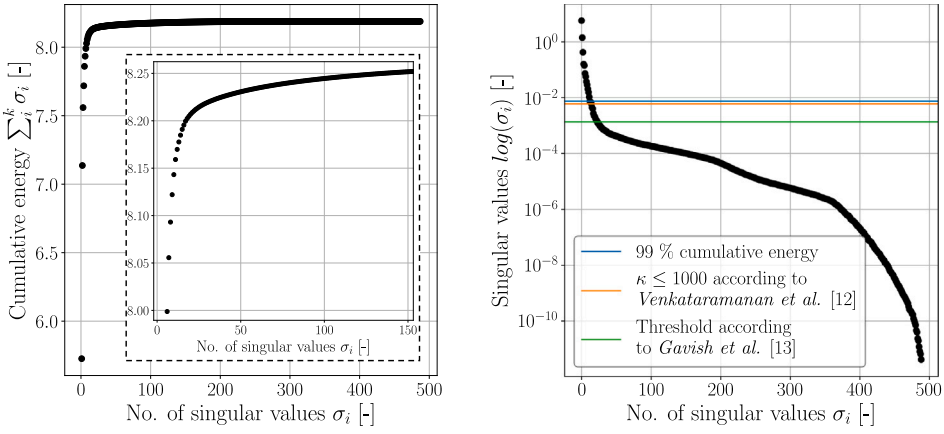

Fig. 2. Cumulative energy (left) and absolute value (right) of singular values in Σ. Right graph also depicts optimal thresholds for r determined with three different methods.

constrain the condition number of the matrix $\kappa(X)$ to be close or equal to 10^3 [12], which is defined as:

$$\kappa(X) = \frac{\sigma_{\max}(X)}{\sigma_{\min}(X)} \tag{6}$$

In [13], the authors proposed a method for identifying an optimal threshold for the truncation of the SVD in the context of a low-rank structure of the matrix X, which is contaminated with Gaussian noise:

$$X = X_{\text{true}} + \gamma X_{\text{noise}} \tag{7}$$

For a known noise magnitude γ, there exist closed-form solutions for the hard threshold. However, in the case of non-square matrices X and unknown noise magnitudes, the threshold must be approximated. To do so, the magnitude of noise is estimated assuming a typical S-shaped structure of the singular values and scaling the distribution of the singular values by using the mean singular value. Both the methodological background and related MATLAB code are provided in [13]. Fig. 2 depicts the cumulative energy as well as the absolute value of the singular values for the range of singular values n. As depicted in the left plot of Fig. 2 the cumulative energy content of the first singular values is predominant, which implies that only a few eigenspectra, i.e. column vectors of U_r, are necessary for a sufficient approximation. This assumption is confirmed by the distinct course of the singular values σ_i as depicted in the right plot in Fig. 2. The curve is initially steep, followed by a less pronounced slope and drops significantly for the last singular values, which is a favorable property of the SVD and verifies the assumption of a S-curve shaped distribution of singular values regarding the methodology in [13]. Additionally, the optimal thresholds according to the three introduced methodologies are depicted, which indicate the 14th, 15th and 23$^{\text{rd}}$ singular value. Consequently, the representation of individual EIS measurements can be effectively reduced to less than 5%, which is particularly advantageous for data-driven modeling. As long as the reconstruction basis U_r is not changed, only the low-dimensional representation needs to be stored or exchanged, thus also decreasing the amount of exchanged data, which is beneficial for cloud-based applications. The distinction between the method proposed in [13] and the two other methods is likely attributable to the supposition that the optimal threshold is situated at the point of intersection between the ordinate and the prolonged

shape of the S curve, excluding the initial steep segment. In order to gain a fundamental understanding of the nature and representation of the eigenspectra, Section S2 depicts the initial five columns of the U matrix together with the mean spectrum in X in a Bode diagram.

3. Results and discussion

The initial Section 3.1 outlines the reconstruction capabilities of EIS using the proposed procedure and illustrates their use as a filter, particularly in instances where measurements exhibit fluctuations due to process-related as well as measurement-related noise. In Section 3.2, a three-dimensional representation of EIS in the space of eigenspectra is presented, utilizing all measurements obtained from one of the stack experiments included in X. Section 3.3 is dedicated to the determination of optimal frequencies to enable the reconstruction of complete spectra from sparse sampling of the impedance. In order to verify this approach, the reconstruction of EIS is tested not only for holdout validation measurements, but also for cases of distorted and falsified EIS in Section 3.4. Therefore, a validation measurement is artificially distorted via ECM fit to magnify individual prevailing polarization resistances as well as including additional emerging polarization resistances. Further, the reconstruction of EIS containing known faults is presented as well.

3.1. Reconstruction of EIS from set of eigenspectra

To obtain an impression of the reconstruction quality of new measurements not contained in X, Fig. 3 shows the reconstruction of four impedance spectra recorded under varying conditions but from the same solid oxide cell stack with internal type designation F1004-139 used for validation purposes. The measurements were conducted as an early stage performance characterization. In addition, the mean spectrum is depicted to illustrate that the reconstruction are not performed in some advantageous regime but off the mean. The reconstructions were calculated according to Eq. (5) and with a rank of $r = 12$, i.e. a slight undercut of the values previously defined as an optimal hard threshold. The reconstruction quality indicates that measurements conducted on a stack not contained in X but under similar conditions, which were not used to determine the singular value decomposition, can be reconstructed with a minimal loss of information (mean squared error MSE $(x, \tilde{x}) = 2.32 \cdot 10^{-10} \dots 4.31 \cdot 10^{-11}\,\Omega^2$). This phenomenon can also be observed in EIS measurements exhibiting different stages of degradation, provided that an interpolation between stages is performed. This finding in turn confirms the importance of the variance of the data set X regarding the desired descriptive variables, such as the operating conditions and the degradation stages. One of the key advantages of the SVD is its ability to identify the most pertinent information within a given data set, while simultaneously disregarding any extraneous noise. Accordingly, the reconstruction of measurements contaminated with process-related noise should be equivalent to a filtering process in some sense tailored to the specific EIS measurements contained in X. Among this data, measurements conducted in humidified H_2 are prone to instabilities due to the fluctuations in steam supply, since the relatively small steam flows are off the design point of the electrical steam generators. Such instabilities can resemble uniformly distributed process-related noise, as illustrated in Fig. 3-B together with four rank-r reconstructions of the measurement conducted at 700°C in humidified H_2. The progressive enhancement in reconstruction precision with rising rank r (mean squared error MSE $(x, \tilde{x}) = 4.29 \cdot 10^{-9}, 1.09 \cdot 10^{-9}, 3.51 \cdot 10^{-10}$ and $2.39 \cdot 10^{-10}\,\Omega^2$, for ranks $r = 2$, 5, 10 and 20, respectively) evinces a comparably steep increase compared to that observed between the cumulative energy and the singular values, as depicted in the left plot of Fig. 2. The aforementioned capability of the reconstruction basis as a filtering algorithm is most evident in the low-frequency range, where steam flow-induced fluctuations are observable. In addition, outliers can be filtered out very efficiently, although it should be emphasized that the initial preparation including the curation of such instabilities from the data set X is crucial and elaborated in [18]. Further, it is noticeable that the incorporation of different eigenspectra seem to affect different frequency regimes of the spectrum to a varying extent. The high-frequency part, for example, is only sufficiently represented from $r > 5$ on, while the plateau in the medium frequency range and the low-frequency arc are already well approximated. A comparison of the magnitude of the first five eigenspectra over the frequency revealed that U_{1-3} contain the most similarity and are therefore more comparable to the average spectrum $\bar{x}$, for instance. U_4 and U_5, on the opposite, mostly affect the low and high frequency parts of the magnitude, respectively. To visualize these peculiarities of U_{1-5} Section S2 depicts these in a Bode diagram.

3.2. Low dimensional representation of EIS in the space of eigenspectra

Since every permutation of orthonormal vectors in U_{ijk} spans a vector space, EIS measurements can be depicted in a three dimensional latent space. Fig. 4 for instance, shows the space spanned by the first three column vectors U_{123} containing all EIS measurements conducted during a 2-layer SOC stack long-term experiment with internal designation F1002-204, depicted as colored dots. The stack was subjected twice in succession to operation in five defined load phases with a current density of at least $1.0\,\mathrm{A\,cm^{-2}}$ and a fuel utilization of at least 70%. Overall, the stack was operated for over 3.400 h under load.

After each load phase, EIS measurements were performed on both layers of the stack under the 4 conditions shown in Fig. 4, yielding up to 22 individual spectra per measurement condition. Noticeably, the low-dimensional representation of different measurements exhibits distinct clusters corresponding to the measurement conditions. Regarding the physical significance that can be attributed to the individual eigenspectra U_i, there are clear correlations between the axes U_{123} and the temperature, humidity content and degradation progress. The latter can be deduced from the temporal evolution of the individual measurements, i.e. the degradation trend, along the dashed arrow shown in Fig. 4-B, independent of the measurement conditions. Furthermore, this low-dimensional representation is also suitable for identifying faulty states. During the above-mentioned experiment a leakage was identified on the upper layer of the stack, which is evident in the open circuit voltage (OCV) and the corresponding EIS measurement. This alteration of the spectrum, particularly in the low-frequency semicircle, also changes the low-dimensional representation, with the result that those measurements move towards the region of the measurements conducted in humidified H_2, as marked in Fig. 4-A by a dashed ellipse. These measurements differ from the others and tend to form an independent cluster. Such properties suggest an application of this latent space for data-driven classification and regression tasks in the context of performance and failure prediction of SOC stacks, which is the subject of future work. A particularly appropriate set of features for such tasks is the projection of individual spectra onto the respective eigenspectra U_i, in this sense displaying the exact proportion of the respective eigenspectra that make up the specific spectrum. This already mentioned *fingerprint* of a new measurement $U^T_{r=1\dots9}(x - \bar{x})$ is depicted in Fig. 5 for various measurements conducted at different degradation stages and measurement conditions, over the first nine eigenspectra. The measurements shown were all acquired on the two-layer long-term stack experiment with type designation F1002-204, also depicted in Fig. 4. The initial stage corresponds to the initial characterization, the intermediate to that after the first completion of the five operating phases and the final to that after the repetition of the five phases mentioned above. As already assumed by Fig. 4, major differences can be observed with regard to various measurement conditions, also at the same degradation stage, although this mainly applies to approximately the first five eigenspectra. However, distinct patterns are observable which in the case of image recognition tasks are used very effectively to train classifiers [11, pp. 178]. The latter is especially interesting for early stage detection of failures, such as a leakage, as identified

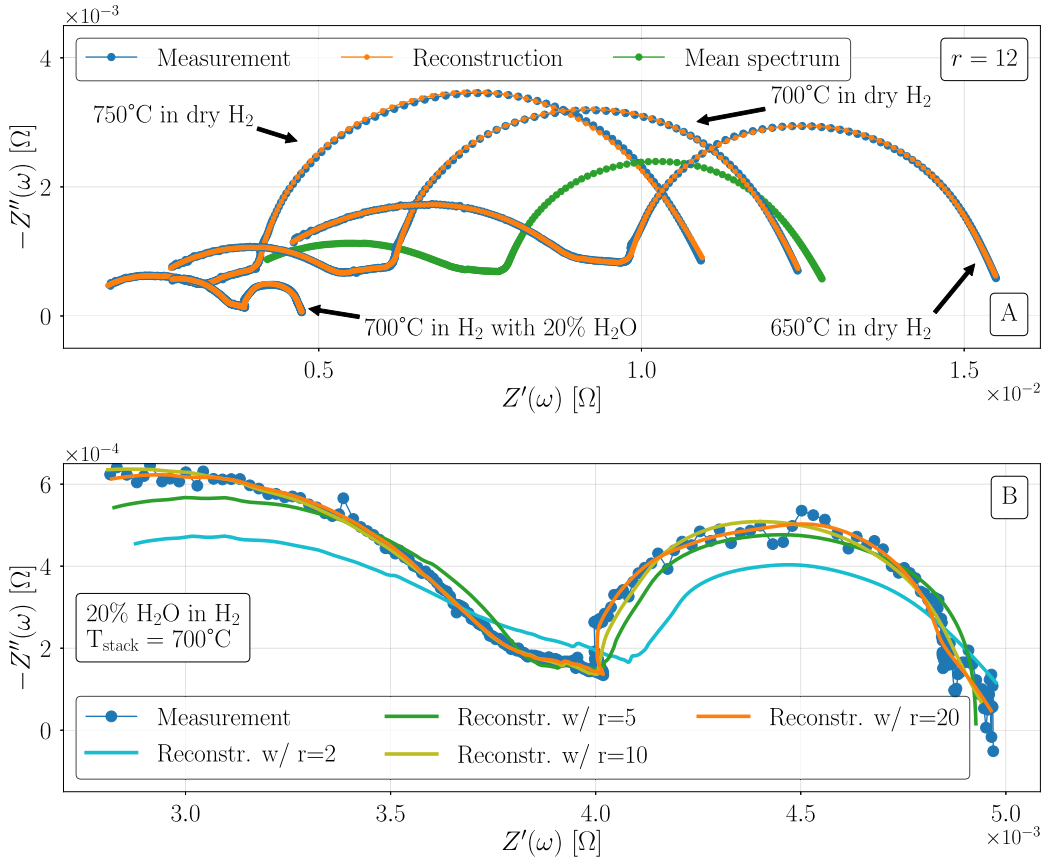

Fig. 3. A: Reconstruction of spectra conducted on same stack layer at various measurement conditions performed with rank $r = 12$ of U_r. B: Measurement conducted in humidified H_2 at 700°C together with reconstructions using four different ranks r of U_r.

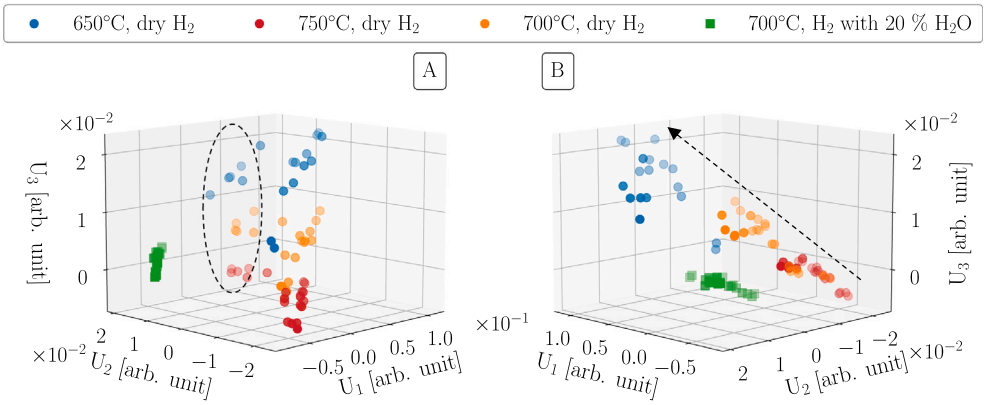

Fig. 4. Low-dimensional representation of all EIS measurements conducted on a two layer stack with internal type designation F1002-204.

on cell 2 of F1002-204 during the first repetition of the five phases by a significantly reduced OCV in addition to the typical decrease of the low-frequency semicircle in the respective EIS. The OCV at 750°C in dry H_2 for cell 1 and 2 was 1225 mV/1203 mV at the initial stage, 1223 mV/1161 mV at the intermediate stage and 1219 mV/1118 mV at the final stage. This trend of an increasing leakage is also reflected by the temporal change in the *fingerprint* of both cells, especially with respect to the first two eigenspectra. While a smaller decrease in the projection onto the first eigenspectrum U_1 can be observed for those measurements conducted in dry H_2 on cell 2, a stronger decrease in the projection onto the second eigenspectrum U_2 is noticeable. This behavior leads directly to the spectra encircled in Fig. 4-A, which have been identified as containing a leakage. In addition, the projections on the other eigenspectra $U_{i>3}$ show partly uniform and partly opposing changes between the two cells, depending on the measurement conditions. Even if the changes are comparatively small, the projections on $U_{4,5}$ appear to drop more sharply with decreasing measurement temperature, considered over time and for the measurements in dry H_2. This observation is only valid to a limited extent for the measurements in humidified H_2, which in turn show no clear behavior with regard to the projection on $U_{4,5}$. This is particularly evident in the case of U_4, which has been observed to exert a significant influence on the low-frequency regime of the spectrum. In contrast to EIS measurements conducted in dry H_2 the latter is less affected by the observed leakage in EIS with humidified H_2. A particularly important task for practical applications is the early identification of fault patterns, such as for cell 2

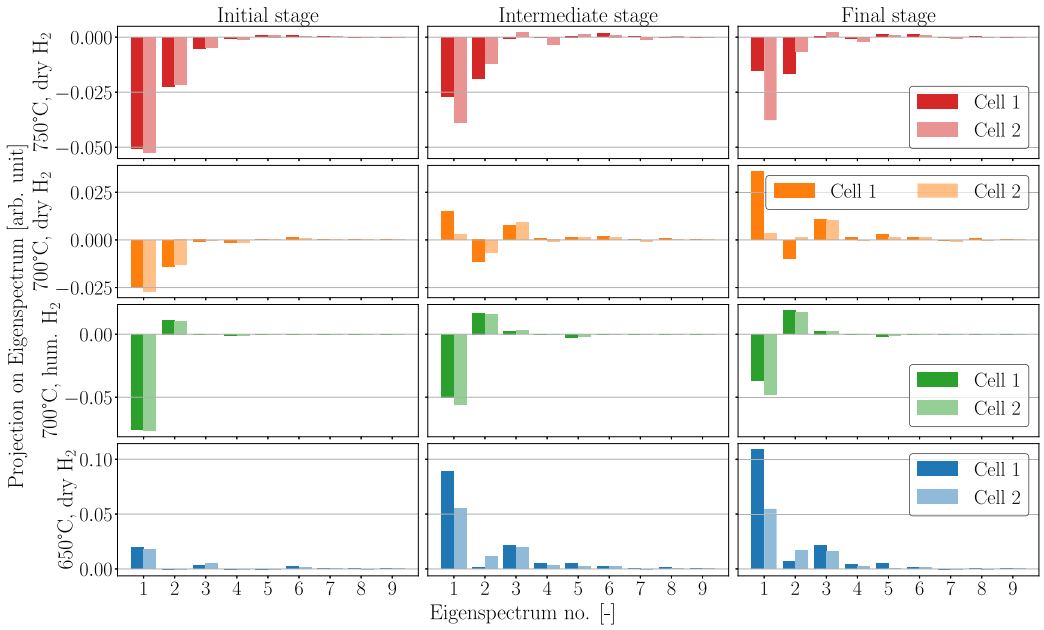

Fig. 5. Projections of EIS spectra onto the first nine eigenspectra of U. Measurements conducted at different conditions and different stages of degradation of stack F1002-204.

in Fig. 5, and the estimation of their probability during operation. One hurdle, however, is the necessity of uniquely labeled reference measurements with the respective fault patterns, besides leakages. Within the consolidated set of EIS measurements X, there is a near-exclusive superposition of fault patterns and degradation phenomena, such that there are few unambiguously labeled measurements. To attain spectra with distinctly high projections on specific eigenspectra, assuming these to represent a specific fault pattern, one could try to sample spectra in distinct regions or along specific axes of the three dimensional latent space in Fig. 4. This does inevitably result in inverting a reconstruction matrix with $U \in \mathbb{R}^{n\times m}$ and $n \gg m$, which is possible by means of the Moore–Penrose pseudo inverse [22], for instance, but results in very unsatisfactory reconstruction quality due to the neglect of the remaining values for $U_{i>3}$. Therefore the alteration of validation EIS measurements by means of an ECM fit (cf. Section 3.4) will be performed to attain specifically falsified spectra for the identification of fault patterns in future works. Calculated or simulated EIS were already successfully chosen in literature to attain a sufficient data set, as in [23] for instance, to correlate EIS with specific faults.

3.3. Reconstruction of EIS from tailored measurements at few frequencies

A significant reduction in the complexity of sine-sweep based EIS, with the objective of achieving near-industrial application, would entail the measurement of only few particularly relevant frequencies and the reconstruction of the entire spectrum from these. The observation that in a set of EIS measurements X there exist intrinsic eigenspectra U_i, of which only few are necessary for the sufficiently accurate approximation $\widetilde{X}$ of all spectra in the data set raises the question of whether this also applies to individual frequencies. Therefore, this section covers the approach to ascertain frequencies, which are sufficient to measure for an accurate reconstruction of measurements conducted on additional DUTs not included in X, but with similar material combinations. The underlying task is referred to as reconstruction from sparse measurements in literature and is closely related to optimal sensor positioning. [7] gives an excellent introduction into the topic with different example applications. The aim in the present case is to calculate a high-dimensional reconstruction $\tilde{x}$ from a low dimensional measurement y of the impedance conducted at specific frequencies $f_i \in \hat{f}$, which are to deduce from the basis of eigenspectra U_r. In such cases, where known patterns in the measured data are exploited to measure the specifically best sensor positions p instead of random positions, the underlying task is also referred to as tailored sensing as described in [7]. Following this procedure, a measurement matrix $C \in \mathbb{R}^{r\times n}$ is introduced, which is intended to define the optimal frequencies at which to sample the impedance. Therefore, each row in C contains a unit entry in the specific column corresponding to f_i and zeros elsewhere, since the values in the columns are arranged in ascending order of the measurement frequency (cf. Eq. (1)). The real and imaginary parts in Eq. (1) were deliberately stacked vertically in order to consider them as separate measurement positions, which has considerable advantages, as will be shown subsequently. According to [7] the optimal position of the unit entries in the measurement matrix C can be determined via formulation of an optimization problem, for a given rank r:

$$a = \arg\min_{a'} \|a'\|_1, \quad s.t. \quad y = CU_r a' = \theta a' \tag{8}$$

The variable a represents the linear combination of columns of C and U_r, to retrieve the best possible reconstruction only using the $p = r$ number of tailored sensors. As [7] show, the goal is to minimize the condition number of the θ matrix in order to ensure a stable inversion, which is necessary for reconstruction of individual measurements, as shown subsequently. Further, the authors show that the optimal sensor locations defined by C can be determined by means of the pivoted QR-factorization [24], which controls the condition number by minimizing the matrix volume, whereas the pivot locations in C^T are the optimal sensor positions p to sample the impedance spectrum x at:

$$U_r^T C^T = QR \tag{9}$$

This relationship results from the fact that the pivoting procedure is a greedy approximation of Eq. (8), whereby the pivot positions are precisely the column vectors of U_r^T that are more relevant to the procedure. Which in this case is the maximum two-norm related to the previous pivot column vector in order to maximize the sub-matrix volume. A major advantage of this method is the simplicity of application, since the QR-factorization is ubiquitous and well implemented in almost all programming frameworks. A recent example is the implementation to determine optimal sensors for structural health monitoring in buildings from reconstruction of dynamic responses, as investigated in [25] and closely related to the present task. In the present work, the sensor positions p, namely the frequencies f_i at which to sample the impedance, are directly deduced from the reconstruction basis U_r. Using only these

frequencies, a high-dimensional reconstruction $\widetilde{x}$ can be determined from a low-dimensional measurement y. Specifically, this is achieved by multiplying the reconstruction basis of rank r with the variable a, which represents the optimal linear combination of C and U_r as defined in Eq. (8). The variable a in turn can be assessed by inverting the matrix θ as depicted in Eq. (10). Consequently, the high-dimensional reconstruction $\widetilde{x}$ can be traced back to the reconstruction basis U_r, the measurement matrix C, and the low-dimensional measurement y at the specific frequencies f_i encoded in C:

$$\widetilde{x} = U_r a = U_r \theta^{-1} y = U_r (C U_r)^{-1} y \tag{10}$$

Fig. 6-A depicts both the original spectrum, as well as the high-dimensional reconstruction of a validation EIS measurement not included in the data set X to verify the reconstruction capabilities. Apart from the mean spectrum in X the sensor positions p, namely the uniquely identified frequencies are depicted as well. As previously mentioned, the real and imaginary parts of the impedance are theoretically considered as different sensors. As a result, two sensor positions can almost coincide if one measures the real and the other the imaginary part at a particular frequency f_i, as can be seen in Fig. 6-A. Of course, this is only a theoretical and not a practical assumption. However, by manually adjusting exactly these positions, it is possible to acquire two sensor positions with the same frequency. The number of sensor positions p is counted by the number of uniquely measured frequencies. By this means, the number of sensor positions can be reduced to $p \geq r/2$ as depicted in Fig. 6-B, while maintaining a similar reconstruction quality, since the rank of U_r did not change. Only the measurement matrix C must be adapted to include a unit entry for the real part and one for the imaginary part in the column vectors assigned to the respective frequencies f_i (cf. Eq. (1)). This reduction in the number of necessary point sensors is highly advantageous for the practical applicability of this method and undercuts the theoretical lower limit of $p = r$ described in [7]. Nevertheless, the manual adjustment of frequencies is incongruous with the original optimality, as evidenced by a divergent reconstruction quality of measurements conducted under specific measurement conditions. Naturally, for an application that is suitable for regular use in determining simplified EIS, it is essential to demonstrate accurate reconstructions from tailored impedance measurements for a subset or even for all measurement conditions and especially for all DUTs. To find a set of locally optimal frequencies, considering only specific measurement conditions, and globally optimal frequencies, taking into account all measurement conditions in the data matrix X, the respective frequencies f_i must not be determined via manual adjustment of the measurement matrix C as done above. Instead, an optimization approach subject to a subset of EIS measurements $\hat{X} \subset X$ and the desired number of frequencies, i.e. the sensor positions $p = r/2$, is proposed. The subset $\hat{X}$ can include every permutation of measurement conditions or degradation stages, but within this work only the main measurement conditions depicted in Fig. 1 will be considered separately.

The optimality of individual frequencies f_i given a reconstruction matrix with rank $r = 2i$ is evaluated by minimizing the mean squared error (MSE) between the individual measurements $x_j \in \hat{X}$ and their high-dimensional reconstruction $\widetilde{x}_j$ over the considered frequency range $\hat{f}$. The only hard constraint is the pairwise congruence of one frequency for measuring the real and one for measuring the imaginary part at each sensor position p, i.e. $i = r/2$. The optimization problem as described in Eq. (11) is conducted for the most interesting ranks, namely four to twelve and the frequency range $\hat{f}$ that most EIS measurements in the data set do exhibit (cf. Fig. 1). The optimization is evaluated with GEKKO [26].

$$\begin{aligned} \arg\min_{f_i \in \hat{f}} \quad & \mathrm{MSE}(x_j, \widetilde{x}_j), x_j \in \hat{X} \subset X \\ s.t. \quad & \\ & i = r/2 \in \mathbb{N} \\ & r = [4, 6, 8, 10, 12] \\ & \hat{f} = [10^{-1} \ldots 7.5 \cdot 10^3 \,\mathrm{Hz}] \end{aligned} \tag{11}$$

The outcome is a set of i measurement frequencies f_i for every EIS measurement x in the specific subset $\hat{X}$, yielding the smallest MSE between reconstruction and original measurement. To attain the distribution on which the frequency of occurrence of individual measurement frequencies f_i is based, a bootstrap procedure with $n_{res.} = 1000$ resamples is conducted. For instance, Fig. 7 depicts the bootstrap distribution for all 857 EIS measurements in X conducted at 700°C in dry H_2 (cf. Fig. 1: the remaining 12 EIS belong to the holdout validation stack) over the frequency range $\hat{f}$ for all ranks r separately. This procedure makes it possible to assess the distribution shape in terms of whether the simplifying assumption can be made that the mean value of the distribution represents it well. As can be seen in Fig. 7 the majority of the distributions do exhibit a form close to a Gaussian normal distribution, thus the mean frequency of each distribution can be considered as the optimal frequency within the specific range. The frequencies identified as optimal for all subsets $\hat{X}$ in this manner are abbreviated as f_i^* in the following. The resulting bootstrap distributions are presented in Sections S3-S7, accompanied by the respective reconstruction of validation measurements using the identified optimal frequencies f_i^* for each measurement condition individually and finally for the complete data set X, thus all measurement conditions combined. A review of Fig. 7 reveals that the distributions are predominantly localized in the gray shaded areas, which indicate the expected locations of the respective peaks of the distribution of relaxation times (DRT) deconvolution. This observation lends further support to the physical meaningfulness of the proposed procedure, which is substantiated when considering the reconstruction quality achieved with the frequencies f_i^* identified from the bootstrap distributions depicted in Fig. 7. These are depicted in Section S5 for the application of validation measurements conducted at 700°C on the holdout SOC stack as also employed for the remaining measurement conditions outlined in Sections S3-S7. The respective validation measurements were conducted after 2,400 h of fuel cell operation under load with at least 0.8 $\mathrm{A\,cm^{-2}}$ and at least 70% fuel utilization. For Fig. 7, it is noteworthy that the distributions between 10^0 and 10^1 Hz for $r = 8$ and $r = 10$ exhibit a comparatively pronounced widening and less Gaussian shape. A comparison with the reconstructions depicted in Fig. S6 indicates that the mentioned frequency range can be allocated to the leftmost end of the low-frequency semicircle. This frequency range is prone to varying faults, as comprehensively described in [23] for the case of fault prediction from EIS, where exactly this range could be identified as most influential. The varying degradation stages represented by the EIS in X, including the presence of faults with varying degrees of severity, provide a plausible explanation for the ambiguity observed in the respective frequency range. Besides other factors as fluctuations during the EIS measurement which are mostly observable in the low-frequency range, a reason on the procedural side could be the comparatively high weighting of the MSE by the low-frequency arc. In addition, despite the comparatively high 50 frequencies per measurement decade, the density of the measurement frequencies is significantly lower than in the high-frequency part. It is therefore likely that such ambiguous form of distributions will also manifest primarily in the frequency range 10^{-1} to 10^1 Hz, along with the other measurement conditions, as illustrated in Sections S3-S7. A comparison with the specified sections confirms exactly this assumption. It is noteworthy that as the rank increases, the distribution becomes increasingly narrower, thereby facilitating a more definitive estimation of the optimal frequency f_i^* for each distribution. This effect is particularly noticeable when determining the optimal frequencies for all measurements contained in X (cf. Section S7).

3.4. Reconstruction of distorted and corrupted EIS from sampling at f_i^*

A crucial aspect towards practical implementation of the proposed method is the precise reconstruction of unseen or distorted EIS from tailored sensing, in particular. Such a distortion or corruption could be induced from excessive deterioration due to operation, known fault

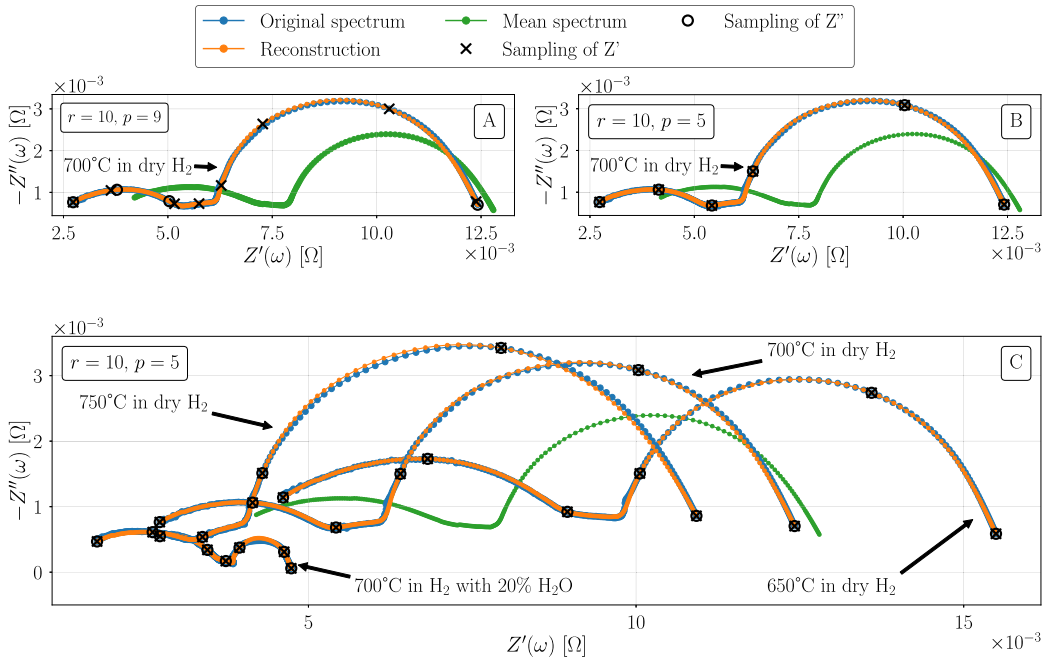

Fig. 6. Reconstruction of sample EIS spectrum conducted in dry H_2 at 700°C from low-dimensional measurement at initial (A) and optimized point sensors p (B). Reconstruction of sample EIS spectra at various measurement conditions from sparse measurement at point sensors p (C).

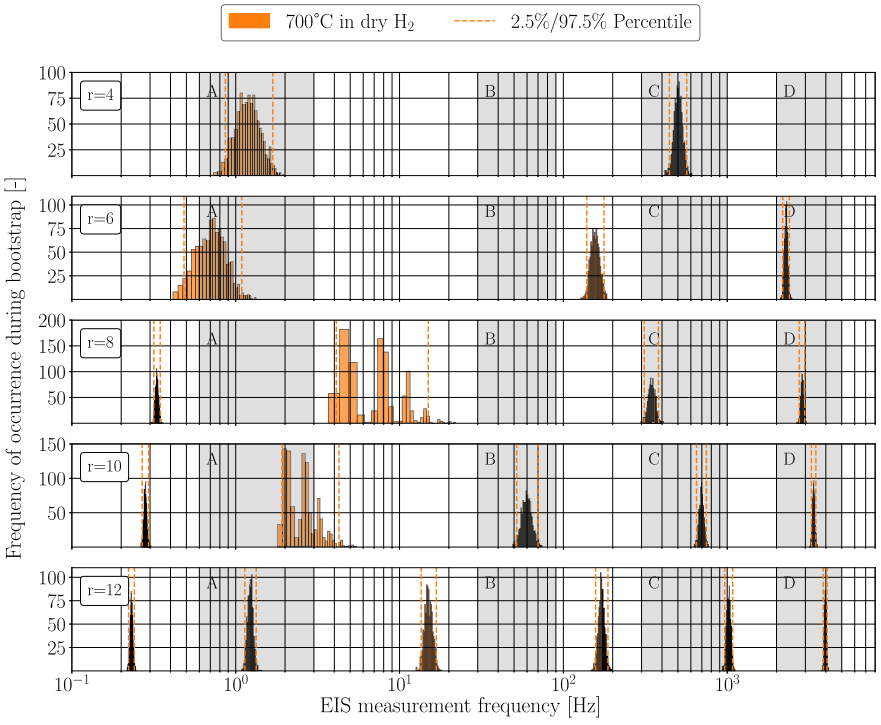

Fig. 7. Bootstrap distribution of frequencies f_i identified for all EIS measurements in X conducted at 700°C in dry H_2 (cf. Fig. 1) for varying ranks r of reconstruction matrix U_r. Gray shaded areas indicate typical ranges of DRT peak-to-process attribution [27] of: Gas conversion peak (A), oxygen electrode peak (B), fuel electrode diffusion peak (C) and fuel electrode charge transfer peak (D).

patterns on individual stack layers (such as a leakage or loss of contact) or even a failure on stack or system level, such as a gradient in temperature or fuel supply during the EIS measurement. The unforeseen occurrence of additionally emerging polarization resistances or the implausibly high change of latter is particularly interesting to observe, as such measurements are barely contained in the data set. Due to this scarcity, it is conceivable to artificially adjust a validation measurement using an ECM fit in such a way that the desired distortion is created. For

this purpose, one of the holdout validation measurements, performed at 700°C in dry H_2 during the initial characterization of the stack experiment was chosen for ECM modeling to ensure a pristine reference state. The ECM consisted of a high-frequency series resistance (R_s), an inductance (L) and four series-connected elements of resistance and constant phase element (RQ) and is often used in literature to fit SOCs [28]. The ECM fit was carried out up to a frequency of 30 kHz instead of 7.5 kHz in order to take sufficient account of the high-frequency influence. However, the reconstructions were only performed up to 7.5 kHz. Subsequently, each of the four resistances of the RQ elements was increased by 100%, while the remaining resistances were maintained at their original values. The resulting spectra were then sampled with the optimal frequencies f_i^* determined for all EIS in X to provide the most general application and reconstructed with the original reconstruction matrix U_r. In addition, both in the high and low frequency regime a RQ-element was inserted individually to also cover an additionally emerging polarization resistance. The additional elements, designated RQ_{lf} and RQ_{hf}, respectively, exhibit identical characteristics to those of RQ_4 and RQ_1, with the exception that the resistance in RQ_{lf} was chosen to be half of that in RQ_4. For each of these six scenarios Fig. 8 depicts the original ECM fit, the fit of the distorted ECM as well as the reconstruction of latter determined for a rank of $r = 12$. The corresponding graphs for lower ranks can be found in Section S8. Given that the distorted spectra are not included in X, the reconstructions exhibit a noteworthy degree of accuracy. This is particularly evident in the case of RQ_3 and RQ_{hf}, where the magnification and insertion of polarization resistances has resulted in a pronounced distortion. However, this accuracy markedly declines at lower ranks, such that for $r = 6$, only RQ_{hf} exhibits a notable alignment, primarily due to the disparate frequency ranges of the distorted ECM fit and the reconstruction. As previously observed for Fig. 7, the frequencies f_i^* identified as optimal for $r = 12$ are only partly situated within the gray shaded areas where the corresponding DRT deconvolution peaks would be expected. This observation also holds true for the optimal frequencies f_i^* identified for all measurements in X, as depicted in Fig. S10. The frequencies are distributed in a relatively uniform manner, occupying positions between the specified DRT ranges. In the present case, this distribution is advantageous because it facilitates the reconstruction of the transition between the initial and distorted ECM components with precision. The aforementioned behavior appears to diminish in cases where $r = 10$ (cf. Figs. S10, S13), wherein the optimal frequencies are predominantly situated within the respective DRT ranges. However, a direct comparison is not feasible due to the varying ranks. A notable observation regarding the left shoulder of the low-frequency arc is that it is reconstructed with greater deficiencies, not only for the case of an distorted low-frequency polarization resistance (RQ_4/RQ_{lf}), but also for the case of a distorted high-frequency arc, specifically in relation to RQ_1 and RQ_{hf}. The mentioned inaccuracy decreases for the next lower rank, since here the measured frequency is closer to the mentioned left shoulder, but at the expense of a lower reconstruction quality in other parts (cf. Fig. S13). In the case of rank $r = 12$, it appears that the objective is to replicate the mean ratio between high and low frequency semicircles encoded in X. This assumption is substantiated by the curvature in the referenced left shoulder of the low-frequency semicircle, which exhibits a significant change in curvature for RQ_1 and RQ_{hf}, as if, starting from this area, the arc should have been larger. This phenomenon is particularly pronounced in RQ_4, where the ratio between the low- and high-frequency semicircles is most markedly altered. This observation raises the question of whether the addition of artificially adjusted spectra to the data set could potentially enhance the reconstruction quality of EIS measurements that contain faults or distortions as depicted in Fig. 8. This question will be addressed in future work, especially as it could improve another very practical challenge, namely the reconstruction of EIS measurements affected by known or unknown fault patterns, sampling just from those frequencies f_i^* identified as optimal for all EIS in X. Such fault patterns include internal damages such as electrical short circuits and contact losses or leakages, as well as external influences such as variations in operating temperature or gas supply during the measurement. Section S9 presents two internal and two external faults observed in EIS measurements on stack level, as well as the corresponding reconstructions for varying ranks r. In conclusion, it can be stated that faults which do not contravene the Kramers–Kronig validity [29], particularly the time-invariance, can be approximated with a sufficient degree of accuracy. An EIS measurement conducted with a feed gas gradient was not adequately reconstructed, which was indicated by an insufficient accuracy in the low frequency arc. In comparison, a measurement comprising a temperature drift can be reconstructed with greater accuracy. It can be observed that a widening of the low-frequency semicircle can be approximated with greater precision than a significant increase in curvature, thus resulting in a hook shape. However, in consideration of the substantially shorter measurement time achieved by the proposed method, the impact of relatively moderate gradients, such as those subjected to the EIS measurements, should be minimal.

4. Concluding remarks

This work proposes a methodology that allows the reconstruction of the EIS from sparse sampling of the impedance at only a few relevant frequencies. Therefore, a set of over 2,600 EIS measurements conducted on SOC stacks at Forschungszentrum Jülich GmbH containing various measurement conditions and degradation stages has been decomposed using the SVD. The measurements were carried out on 16 different stacks with similar material combinations, which were subjected to more than 47,000 h of operation in fuel cell, electrolysis and co-electrolysis mode, as well as thermal cycling. Prior to analysis the data has been pre-processed and curated from recurrent instabilities using an approach introduced in a prior work [18]. The following conclusions were reached:

1. Less than 5% of the singular values of the SVD are relevant and therefore sufficient for accurate description and reconstruction of the data set. The space spanned by these, in this work referred to as, eigenspectra provides a descriptive low-dimensional representation of individual EIS measurements. In particular, the representation allows for the assignment of different aging stages, measurement conditions, and the presence of fault patterns, such as leakages.
2. Depending on the number of utilized eigenspectra r a set of $r/2$ frequencies could be identified to sparsely sample the impedance at and reconstruct complete impedance spectra from. Bootstrap distributions to identify the optimal frequencies as a function of r and given all EIS measurements in the data set conducted at specific conditions indicate distinct ranges, which do align with typical ranges of DRT peak-to-process attributions.
3. Reconstruction capabilities on a holdout validation stack with similar material combinations indicate high accuracies for all measurement conditions in the original data set. As expected, the accuracy increases with r, but sufficient reconstructions are already achieved by sampling three optimal frequencies, i.e. $r = 6$.
4. The generalizability of the proposed method was verified by means of artificially deteriorated EIS by ECM fit, which were not included in the initial data set, either. The reconstructions were calculated using those frequencies identified as optimal for all conditions in the data set, thus excluding a biased choice based on the conditions the distorted measurements were recorded at. Reasonable agreements were achieved for $r = 10$, whereby the spectrum was also sufficiently reproduced with $r = 8$, although with reduced accuracy in the low-frequency part.

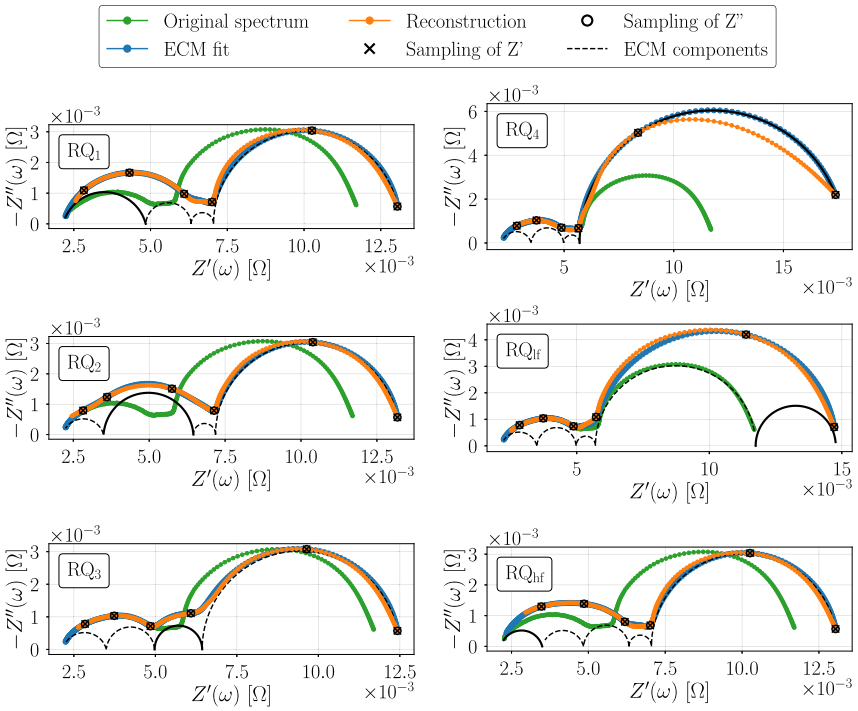

Fig. 8. Reconstruction of artificially distorted spectra by sampling the impedance at optimal frequencies f_i^* evaluated for all measurements in X for rank $r = 12$. Magnified or added ECM components are displayed as solid black line, while other ECM components are indicated as dashed lines. ECM fit (blue) displayed for frequency of up to 30 kHz, reconstructions evaluated up to 7.5 kHz. Validation measurement conducted at 700°C in dry H_2 on holdout validation stack.

5. Accounting for corrupted EIS measurements the reconstruction of EIS comprising recurrent faults, such as a loss of electrical contact between layers, an external leakage, and measurements comprising feed gas and temperature gradients, was verified as well. Using the as optimal identified frequencies for all measurement conditions in the data set, sufficient reconstructions were achieved with $r = 10$.
6. In contrast to state-of-the-art fast impedance methods such as PRBS or PIS the proposed method does not necessarily rely on hardware with high bandwidth and further allows for a readjustment of the specific measurement frequencies. By constraining the frequency in the proposed optimization procedure, for instance, it is possible to avoid measuring the low-frequency part and therefore enable time-efficient measurements, comparable to the mentioned methods.

Overall, the results suggest that an additional enrichment of the data set, potentially through the use of artificially altered EIS via ECM fit of existing measurements, could further enhance the reconstruction capabilities. This approach is the subject of future work, which will combine the proposed method for tailored EIS with the training of data-driven performance prediction models utilizing the low-dimensional representation proposed in this work.

CRediT authorship contribution statement

Christian Mänken: Writing – original draft, Visualization, Validation, Software, Methodology, Data curation, Conceptualization, Formal analysis, Investigation. **Dominik Schäfer:** Writing – review & editing, Supervision, Project administration, Conceptualization, Methodology. **Rüdiger-A. Eichel:** Writing – review & editing, Supervision.

Declaration of competing interest

The authors declare the following financial interests/personal relationships which may be considered as potential competing interests: Christian Frederik Maenken, Dominik Schaefer, Felix Kunz and Ruediger-A. Eichel has patent #DE Application No. 102024200774.9 pending to Forschungszentrum Jülich GmbH. If there are other authors, they declare that they have no known competing financial interests or personal relationships that could have appeared to influence the work reported in this paper.

Acknowledgments

The authors would like to thank their colleagues at Forschungszentrum Jülich GmbH for their great support and the Helmholtz Society as well as the German Federal Ministry of Education and Research for financing these activities as part of the WirLebenSOFC project (03SF0622B).

Appendix A. Supplementary data

Supplementary material related to this article can be found online at https://doi.org/10.1016/j.jpowsour.2024.235808.

Data availability

Data will be made available upon reasonable request.

References

[1] A. Nechache, M. Cassir, A. Ringuedé, Solid oxide electrolysis cell analysis by means of electrochemical impedance spectroscopy: A review, J. Power Sources 258 (2014) 164–181, http://dx.doi.org/10.1016/j.jpowsour.2014.01.110.

[2] J. Sihvo, T. Messo, T. Roinila, R. Luhtala, Online internal impedance measurements of Li-ion battery using PRBS broadband excitation and Fourier techniques: Methods and injection design, in: 2018 International Power Electronics Conference (IPEC-Niigata 2018 -ECCE Asia), IEEE, 2018, http://dx.doi.org/10.23919/ipec.2018.8507565.

[3] A. Fairweather, M. Foster, D. Stone, Battery parameter identification with pseudo random binary sequence excitation (PRBS), J. Power Sources 196 (22) (2011) 9398–9406, http://dx.doi.org/10.1016/j.jpowsour.2011.06.072.

[4] D. Klotz, M. Schönleber, J. Schmidt, E. Ivers-Tiffée, New approach for the calculation of impedance spectra out of time domain data, Electrochim. Acta 56 (24) (2011) 8763–8769, http://dx.doi.org/10.1016/j.electacta.2011.07.096.
[5] J. Mougin, B. Morel, A. Ploner, P. Caliandro, J. Van Herle, P. Boškoski, B. Dolenc, M. Gallo, P. Polverino, A. Pohjoranta, A. Nieminen, S. Pofahl, J.P. Ouweltjes, S. Diethelm, A. Leonardi, F. Galiano, C. Tanzi, Monitoring and diagnostics of SOFC stacks and systems, ECS Trans. 91 (1) (2019) 731–743, http://dx.doi.org/10.1149/09101.0731ecst.
[6] G. Nusev, B. Morel, J. Mougin, Đ. Juričić, P. Boškoski, Condition monitoring of solid oxide fuel cells by fast electrochemical impedance spectroscopy: A case example of detecting deficiencies in fuel supply, J. Power Sources 489 (2021) 229491, http://dx.doi.org/10.1016/j.jpowsour.2021.229491.
[7] K. Manohar, B.W. Brunton, J.N. Kutz, S.L. Brunton, Data-driven sparse sensor placement for reconstruction: Demonstrating the benefits of exploiting known patterns, IEEE Control Syst. Mag. 38 (3) (2018) 63, http://dx.doi.org/10.1109/mcs.2018.2810460.
[8] J.L. Callaham, K. Maeda, S.L. Brunton, Robust flow reconstruction from limited measurements via sparse representation, Phys. Rev. Fluids 4 (10) (2019) 103907, http://dx.doi.org/10.1103/physrevfluids.4.103907.
[9] H. Abdi, L.J. Williams, Principal component analysis, WIREs Comput. Stat. 2 (4) (2010) 433–459, http://dx.doi.org/10.1002/wics.101.
[10] A. Chatterjee, An introduction to the proper orthogonal decomposition, Curr. Sci. (2000) 808–817.
[11] S.L. Brunton, Data-Driven Science and Engineering, Cambridge University Press, Cambridge, 2019,
[12] L. Venkataramanan, Y.-Q. Song, M. Hurlimann, Solving Fredholm integrals of the first kind with tensor product structure in 2 and 2.5 dimensions, IEEE Trans. Signal Process. 50 (5) (2002) 1017–1026, http://dx.doi.org/10.1109/78.995059.
[13] M. Gavish, D.L. Donoho, The optimal hard threshold for singular values is $4/\sqrt{3}$, IEEE Trans. Inform. Theory 60 (8) (2014) 5040–5053, http://dx.doi.org/10.1109/tit.2014.2323359.
[14] L. Mao, L. Jackson, S. Dunnett, Fault diagnosis of practical polymer electrolyte membrane (PEM) fuel cell system with data-driven approaches, Fuel Cells 17 (2) (2016) 247–258, http://dx.doi.org/10.1002/fuce.201600139.
[15] D. Ritzberger, J. Höflinger, Z.P. Du, C. Hametner, S. Jakubek, Data-driven parameterization of polymer electrolyte membrane fuel cell models via simultaneous local linear structured state space identification, Int. J. Hydrog. Energy 46 (21) (2021) 11878–11893, http://dx.doi.org/10.1016/j.ijhydene.2021.01.037.
[16] L. Blum, H. Buchkremer, S. Gross, A. Gubner, L.G.J.B. de Haart, H. Nabielek, W.J. Quadakkers, U. Reisgen, M.J. Smith, R. Steinberger-Wilckens, R.W. Steinbrech, F. Tietz, I.C. Vinke, Solid oxide fuel cell development at Forschungszentrum Juelich, Fuel Cells 7 (3) (2007) 204–210, http://dx.doi.org/10.1002/fuce.200600039.
[17] Q. Fang, L. Blum, R. Peters, M. Peksen, P. Batfalsky, D. Stolten, SOFC stack performance under high fuel utilization, Int. J. Hydrog. Energy 40 (2) (2015) 1128–1136, http://dx.doi.org/10.1016/j.ijhydene.2014.11.094.
[18] C.F. Mänken, J. Uecker, D. Schäfer, L. De Haart, R.-A. Eichel, Impact of electrochemical impedance spectroscopy dataset curation on solid oxide cell degradation assessment, J. Electrochem. Soc. 171 (6) (2024) 064503, http://dx.doi.org/10.1149/1945-7111/ad510c.
[19] M. Murbach, B. Gerwe, N. Dawson-Elli, L.-k. Tsui, Impedance.py: A Python package for electrochemical impedance analysis, J. Open Source Software 5 (52) (2020) 2349, http://dx.doi.org/10.21105/joss.02349.
[20] P. Virtanen, R. Gommers, T.E. Oliphant, M. Haberland, T. Reddy, D. Cournapeau, E. Burovski, P. Peterson, W. Weckesser, J. Bright, S.J. van der Walt, M. Brett, J. Wilson, K.J. Millman, N. Mayorov, A.R.J. Nelson, E. Jones, R. Kern, E. Larson, C.J. Carey, İ. Polat, Y. Feng, E.W. Moore, J. VanderPlas, D. Laxalde, J. Perktold, R. Cimrman, I. Henriksen, E.A. Quintero, C.R. Harris, A.M. Archibald, A.H. Ribeiro, F. Pedregosa, P. van Mulbregt, A. Vijaykumar, A.P. Bardelli, A. Rothberg, A. Hilboll, A. Kloeckner, A. Scopatz, A. Lee, A. Rokem, C.N. Woods, C. Fulton, C. Masson, C. Häggström, C. Fitzgerald, D.A. Nicholson, D.R. Hagen, D.V. Pasechnik, E. Olivetti, E. Martin, E. Wieser, F. Silva, F. Lenders, F. Wilhelm, G. Young, G.A. Price, G.-L. Ingold, G.E. Allen, G.R. Lee, H. Audren, I. Probst, J.P. Dietrich, J. Silterra, J.T. Webber, J. Slavič, J. Nothman, J. Buchner, J. Kulick, J.L. Schönberger, J.V. de Miranda Cardoso, J. Reimer, J. Harrington, J.L.C. Rodríguez, J. Nunez-Iglesias, J. Kuczynski, K. Tritz, M. Thoma, M. Newville, M. Kümmerer, M. Bolingbroke, M. Tartre, M. Pak, N.J. Smith, N. Nowaczyk, N. Shebanov, O. Pavlyk, P.A. Brodtkorb, P. Lee, R.T. McGibbon, R. Feldbauer, S. Lewis, S. Tygier, S. Sievert, S. Vigna, S. Peterson, S. More, T. Pudlik, T. Oshima, T.J. Pingel, T.P. Robitaille, T. Spura, T.R. Jones, T. Cera, T. Leslie, T. Zito, T. Krauss, U. Upadhyay, Y.O. Halchenko, Y. Vázquez-Baeza, Scipy 1.0: fundamental algorithms for scientific computing in Python, Nature Methods 17 (3) (2020) 261–272, http://dx.doi.org/10.1038/s41592-019-0686-2.
[21] C. Eckart, G. Young, The approximation of one matrix by another of lower rank, Psychometrika 1 (3) (1936) 211–218, http://dx.doi.org/10.1007/bf02288367.
[22] E. Moore, On the reciprocal of the general algebraic matrix, Bull. Amer. Math. Soc. 26 (9) (1920) 394–395, http://dx.doi.org/10.1090/S0002-9904-1920-03322-7.
[23] G.T. Le, L. Mastropasqua, J. Brouwer, S.B. Adler, Simulation-informed machine learning diagnostics of solid oxide fuel cell stack with electrochemical impedance spectroscopy, J. Electrochem. Soc. 169 (3) (2022) 034530, http://dx.doi.org/10.1149/1945-7111/ac59f4.
[24] P.-G. Martinsson, G. Quintana OrtÍ, N. Heavner, R. van de Geijn, Householder QR factorization with randomization for column pivoting (HQRRP), SIAM J. Sci. Comput. 39 (2) (2017) C96–C115, http://dx.doi.org/10.1137/16m1081270.
[25] J. Cao, F. Bu, J. Wang, C. Bao, W. Chen, K. Dai, Reconstruction of full-field dynamic responses for large-scale structures using optimal sensor placement, J. Sound Vib. 554 (2023) 117693, http://dx.doi.org/10.1016/j.jsv.2023.117693.
[26] L. Beal, D. Hill, R. Martin, J. Hedengren, GEKKO optimization suite, Processes 6 (8) (2018) 106, http://dx.doi.org/10.3390/pr6080106.
[27] P. Caliandro, A. Nakajo, S. Diethelm, J. Van herle, Model-assisted identification of solid oxide cell elementary processes by electrochemical impedance spectroscopy measurements, J. Power Sources 436 (2019) 226838, http://dx.doi.org/10.1016/j.jpowsour.2019.226838.
[28] S.E. Wolf, L. Dittrich, M. Nohl, T. Duyster, I.C. Vinke, R.-A. Eichel, L.G.J. (Bert) de Haart, Boundary investigation of high-temperature co-electrolysis towards direct CO2 electrolysis, J. Electrochem. Soc. 169 (3) (2022) 034531, http://dx.doi.org/10.1149/1945-7111/ac5e45.
[29] M. Schönleber, D. Klotz, E. Ivers-Tiffée, A method for improving the robustness of linear Kramers-Kronig validity tests, Electrochim. Acta 131 (2014) 20–27, http://dx.doi.org/10.1016/j.electacta.2014.01.034.

Further reading

[1] S.M. Gross, D. Federmann, J. Remmel, M. Pap, Reinforced composite sealants for solid oxide fuel cell applications, J. Power Sources 196 (17) (2011) 7338–7342, http://dx.doi.org/10.1016/j.jpowsour.2011.02.002.